Frontiers of Information Technology & Electronic Engineering
www.jzus.zju.edu.cn; engineering.cae.cn; www.springerlink.com
ISSN 2095-9184 (print); ISSN 2095-9230 (online)
E-mail: jzus@zju.edu.cn

Near-field joint estimation of multi-targets' position and velocity in a terahertz MIMO-OFDM system based on tensor decomposition

Ke LIU[1], Shengfu ZHAO[1], Weixin CHEN[1], Zhen WANG[1], Lingxiang LI[†‡1], Zhi CHEN[1,2], Qiang XU[1]

[1]*National Key Laboratory on Wireless Communications, UESTC, Chengdu 611731, China*

[2]*School of Electrical Engineering and Information, Southwest Petroleum University Chengdu, Sichuan 610500, China*

[†]E-mail: lingxiang.li@uestc.edu.cn

Received June 2, 2024; Revision accepted Sept. 30, 2024; Crosschecked

Abstract: This paper investigates the joint estimation of multi-targets' position and velocity for a terahertz multiple-input multiple-output (MIMO) orthogonal frequency division multiplexing (OFDM) system operating in the near-field based on tensor decompositions. The waveforms transmitted from shared antennas carry communication messages and are orthogonal to each other in the frequency domain. The estimation of the position and velocity of multiple targets in the considered near-field scenario is challenging because it involves spherical wavefronts. On the other hand, a signal model based on spherical wavefronts enables higher resolutions on spatial position, which, if properly designed, can be used to improve the estimation accuracy. In this paper, we propose a CANDE-COMP/PARAFAC (CP) decomposition-based Near-Field Localization (CP-NFL) algorithm for the joint estimation of the position and velocity of multiple targets. In our proposed method, the received signal is expressed as a third-order tensor, based on whose factor matrices we convert the original non-convex optimization problem into a convex one and solve it with CVX tools. Our analysis reveals that the uniqueness of the CP decomposition can be guaranteed and the computational complexity of the proposed method is linear to the sum of the third power of the number of sub-carriers, OFDM symbols, antennas, and targets. Numerical results show that the proposed method has a clear advantage over the existing method in terms of estimation accuracy and computational complexity.

unedited

Key words: THz; MIMO-OFDM; Near-field localization; Velocity estimation; Tensor decomposition
https://doi.org/10.1631/FITEE.2400472 **CLC number:** TN95

1 Introduction

The demand for ubiquitous, reliable, fast, and scalable wireless services is pushing today's radio technology toward its ultimate limits (Akyildiz et al., 2020). In this context, it is natural to continue searching for more bandwidth, which in turn pushes the operation toward higher frequencies. Terahertz communications in the band from 0.1 THz to 10 THz is considered as a highly promising technology for 6G (the sixth generation of wireless communications) and beyond (Akyildiz et al., 2022). Meanwhile, communications and radar systems that used to operate independently, are now evolving toward integrated sensing and communications (ISAC) systems (Zhang JA et al., 2021). Due to the availability of hundreds of gigahertz-spectrum resources, terahertz communications can provide significant communication capacity and high-precision perception, making terahertz ISAC an attractive research topic (Sarieddeen et al., 2021; Chen H et al., 2022).

On the other hand, the use of high frequencies translates into higher path losses per antenna, which can be compensated for by antenna arrays (Xiao et al., 2017). This combination undermines the fundamental far-field assumption of multiple antenna communications, i.e., the wavefronts of radiated waves are locally planar over antenna arrays (Zhao et

‡ Corresponding author
© Zhejiang University Press 2024

al., 2023; Alhafid et al., 2024). Instead, when the detection range is less than the Rayleigh distance of $\frac{2D_R^2}{\lambda}$, where D_R is the antenna aperture and λ denotes the wavelength, the near-field region should be considered and wavefronts of radiated waves are spherical over antenna arrays (Cui et al., 2023; Zhang HY et al., 2022, 2023). This essential feature causes terahertz arrays to possess both azimuth and distance resolutions. Many existing algorithms make use of spherical wavefronts to enhance positioning accuracy (Singh et al., 2016; Chargé et al., 2017; Podkurkov et al., 2018; Zhang XF et al., 2018; Zuo et al., 2019; Pan et al., 2021; Rinchi et al., 2022). Along this line of research, existing works make a trade-off between complexity and parameter estimation accuracy. Specifically, the work several authors (Zhang XF et al., 2018; Zuo et al., 2019; Pan et al., 2021; Rinchi et al., 2022) approximate the signal model in the array near-field using a second-order Taylor expansion to avoid the computational complexity of parameter estimation, while the work of other authors (Singh et al., 2016; Chargé et al., 2017; Podkurkov et al., 2018) utilize precise near-field spherical wave information for positioning, avoiding the loss of detection accuracy caused by model approximation.

However, the aforementioned positioning methods are based on radar chirp waveforms, whereas orthogonal frequency division multiplexing (OFDM) waveforms are more commonly used in communications. Most importantly, in the foreseeable future, mobile communication protocols will continue to be based on OFDM waveforms. In this study, we considered using OFDM waveforms. Due to the differences in signal generation and formats, the principles of parameter estimation based on OFDM waveforms differ from those based on radar chirp waveforms. Specifically, the traditional radar systems first mix the received signal with the reference signal before ADC, based on which they then derive the target's position, azimuth, and velocity by analyzing the relationship between the resulting signal frequency and the propagation time delay (Tsujimura and Mori, 2022). In contrast, the systems based on OFDM waveforms cannot directly decorrelate the signal before ADC because the instantaneous signal is a multi-carrier signal. Instead, the entire broadband signal must be sampled using an ADC, and target positioning, azimuth, and velocity information are further extracted (Gaudio et al., 2019).

In array far-field scenarios, parameter estimation based on OFDM waveforms is already well-established. Works by Liu et al. (2017), Knill et al. (2019), Sanson et al. (2019), Temiz et al. (2021), Tian et al. (2021), and Wan et al. (2023) have, respectively, used the phase differences between sub-carriers, between antennas, and between symbols for position estimation, azimuth estimation, and velocity estimation. However, in array near-field scenarios, the phase difference between antennas is related not only to azimuth but also to the distance between the array and the target. This significantly increases the complexity of parameter estimation (Podkurkov et al., 2021; Sakhnini et al., 2022). Specifically, the work of Podkurkov et al. (2021) used a method of passive sensing at the base station, processed OFDM uplink signals at the base station, and used precise near-field spherical wavefront information to achieve target positioning. The work by Sakhnini et al. (2022) adopted an active sensing method, utilizing time-division OFDM where each antenna transmits OFDM symbols in a time-multiplexed manner. The proposed scheme requires the antenna spacing in the linear uniform array to be within one wavelength to avoid position ambiguity. Additionally, it uses maximum likelihood estimation methods, resulting in high algorithmic complexity.

1.1 Contributions of this paper

Different from the aforementioned works, this paper uses frequency-orthogonal OFDM (FO-OFDM) signals, where the waveform transmitted from each antenna is orthogonal in the frequency domain for the near-field target positioning and velocity estimation. The specific contributions are as follows:

• By transmitting FO-OFDM signals from the transmitting antennas and then combining them at the receiving end, wideband positioning is achieved and positioning accuracy improves. Additionally, by shifting the constraints for ambiguity from the conventional within-one-wavelength antenna spacing (Sakhnini et al., 2022) to the used signal bandwidth, the scanning range of the antennas increases.

unedited

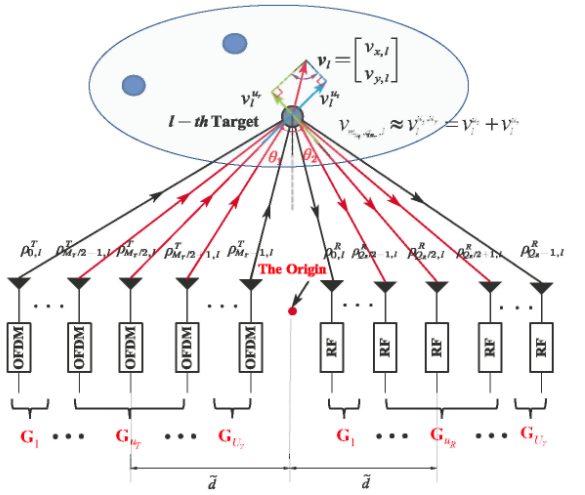

Fig. 1 Illustration of the near-field uniform linear array (ULA) model. OFDM, Orthogonal Frequency Division Multiplexing

• Based on the established near-field signal model, we reconstructed the received data in a tensor third-order form. We then propose a CANDECOMP/PARAFAC (CP) decomposition-based Near-Field Localization (CP-NFL) algorithm, where multi-dimensional information such as phase differences between antennas and phase differences between sub-carriers are jointly processed to enhance the accuracy of target localization estimation.

• Additionally, for the purpose of reducing the complexity of the tensor decomposition algorithm, we separate the transmit and receive arrays into different groups. Analyses show that the computational complexity of the proposed method is linear to the sum of the third power of the number of sub-carriers, OFDM symbols, antennas, and targets. Numerical results show the effectiveness of the proposed method.

Notation: We use lower-case bold letters (e.g., $\boldsymbol{a}$), upper-case bold letters (e.g., $\mathbf{A}$), and bold italic letters (e.g., $\boldsymbol{A}$) to represent the vectors, matrices, and tensors, respectively. $\boldsymbol{a}(i)$ denotes the ith element of a vector $\boldsymbol{a}$. Also, we use $\mathbf{B} = \boldsymbol{a} \circ \boldsymbol{b}$ to denote the outer product between the vectors $\boldsymbol{a} \in C^I$ and $\boldsymbol{b} \in C^J$, which results in a matrix $\mathbf{B}$ of size $I \times J$, $\mathbf{B}_{ij} = \boldsymbol{a}(i)\boldsymbol{b}(j)$. Moreover, $\angle$a denotes the vector of principal angles of complex vector $\boldsymbol{a}$. ||A|| defines the Frobenius norm of matrix $\mathbf{A}$.

2 System model and problem formulation

Consider a multiple-input multiple-output (MIMO) OFDM ISAC system with a uniform linear array (ULA) surveilling the area shown in Fig. 1. The ULA is divided into two groups, where the left group is for the transmitter and the right group is for the receiver, with M_T and Q_R antenna elements, respectively. The antenna element spacing is assumed to be d, and as such, the size of the transmit array and the receive array is equal to $D_T = (M_T-1)d$ and $D_R = (Q_R-1)d$, respectively.

As mentioned previously, for terahertz ISAC systems, the antenna array usually works in the array near-field region, where the spherical wavefront should be considered and the analytical signal model becomes very complex. A hybrid far-field and near-field is considered, where we divide the transmit and receive antenna arrays into U_T and U_R sub-arrays, each of which are equipped with M and Q antenna elements, respectively. Therefore, it holds true that $M_T = U_T M$ and $Q_R = U_R Q$.

The location of the transmitting/receiving antenna is defined in two-dimensional Cartesian coordinates with respect to the origin. Assume that the transmit and receive array are both located on the X-axis. Let the coordinates of the $m_{u_t}^{\text{th}}$ antenna element in the u_t^{th} transmit sub-array and that for the $q_{u_r}^{\text{th}}$ antenna element in the u_r^{th} receive sub-array be, respectively,

$$(x_{T,m_{u_t}}, 0), u_t = 1, \ldots, U_T, m_{u_t} \in ((u_t-1)M, u_t M - 1), \quad (1)$$
$$(x_{R,q_{u_r}}, 0), u_r = 1, \ldots, U_R, q_{u_r} \in ((u_r-1)Q, u_r Q - 1). \quad (2)$$

Specifically, the coordinates of the center antenna element of the transmit/receive array are $(x_{M_T/2}, 0)$ and $(x_{Q_R/2}, 0)$. Let the lth (l=1, ..., L) target locate at (x_l, y_l), whose moving velocity is $(v_{x,l}, v_{y,l})$. In this study, we aimed to estimate the parameters (x_l, y_l), $(v_{x,l}, v_{y,l})$, $\forall$, based on the observed signals reflected from the target.

To accomplish this, the transmitter sends FO-OFDM signals. The FO-OFDM signal contributed from the $m_{u_t}^{\text{th}}$ transmit antenna element contains P symbols and each symbol is composed of N sub-carriers with uniform spacing of Δf. Each OFDM symbol duration is $T_0 = T+T_{\text{cp}}$, where T and T_{cp} denote the duration of the data and guard interval, respectively, for the purpose of avoiding inter-symbol

unedited

interference (ISI) (Zhang et al., 2023). Thus, the waveform transmitted by the $m_{u_t}^{\text{th}}$ transmit antenna at time t is (Gaudio et al., 2019)

$$s_{m_{u_t}}(t) = e^{j2\pi f_c t} \sum_{p=0}^{P-1} \sum_{n=0}^{N-1} \tilde{s}_{m_{u_t},n,p} e^{j2\pi(n+m_{u_t}K)\Delta f(t-pT_o-T_{cp})} \text{rect}\left[\frac{t-pT_o}{T_o}\right], \tag{3}$$

where f_c denotes carrier frequency, p is the OFDM symbols index, and n is the subcarrier index. The symbol $\tilde{S}_{m_{u_t},n,p}$ is modulated on the nth carrier of the pth OFDM symbol for the $m_{u_t}^{\text{th}}$ transmitting antenna. K is an integer whose value should be greater than N such that the waveform from each antenna does not intersect in the frequency domain. The rectangle function rect[t] equals 1 for $t \in [0, T_0]$ and 0 otherwise.

The transmitted signal reaches the receiving end after being reflected by targets. Because the signals transmitted from different antennas are orthogonal in the frequency domain, we consider bandpass filters at the receiver to separate signals from different transmitting antennas. In addition, for the considered terahertz system, the carrier frequency is hundreds of gigahertz, while the signal bandwidth is approximately several gigahertz. The latter is much smaller than the former; consequently in the signal model we only consider the impact of the Doppler frequency shift caused by the carrier frequency and assume a constant Doppler shift over the entire signal bandwidth. The reflected signal from the $m_{u_t}^{\text{th}}$ transmitting antenna to the $q_{u_r}^{\text{th}}$ receiving antenna can thus be expressed as

$$y_{m_{u_t},q_{u_r}}(t) = \sum_{l=1}^{L} \alpha_l e^{j2\pi(f_c+f_l^D)(t-\tau_{m_{u_t},q_{u_r},l})} s_{m_{u_t}}(t-\tau_{m_{u_t},q_{u_r},l}) + z_{m_{u_t},q_{u_r}}(t), \tag{4}$$

where α_l represents the path loss from the transmitter to the receiver related to the lth target, which remains almost constant during the observation time. $f_l^D = \frac{2v_{m_{u_t},q_{u_r},l} f_c}{c}$ is defined as the Doppler shift, where c denotes the speed of light and $v_{m_{u_t}}, q_{u_r}, l$ is the velocity along the wavefront propagation path from the $m_{u_t}^{\text{th}}$ transmit antenna to the $q_{u_r}^{\text{th}}$ receive antenna related to the lth target. It is worthwhile to note that we estimate and observe the velocity based on Doppler shift. For a target moving in the array near-field scenario, the Doppler shift from different signal propagation paths is different. Therefore, the observed velocity is also different. In addition, $\tau_{m_{u_t}}, q_{u_r}, l$ represents the propagation time delay and $z_{m_{u_t}}, q_{u_r}(t)$ denotes the AWGN noise.

Let $R_{m_{u_t}}, q_{u_r}, l$ be the propagation path length from the $m_{u_t}^{\text{th}}$ transmitting antenna to the lth target. After being reflected to the $q_{u_r}^{\text{th}}$ receiving antenna, the propagation time delay of $\tau_{m_{u_t}}, q_{u_r}, l$ can be expressed as

$$\tau_{m_{u_t},q_{u_r},l} = R_{m_{u_t},q_{u_r},l}/c = \left(\sqrt{(x_l - x_{T,m_{u_t}})^2 + (y_l)^2} + \sqrt{(x_l - x_{R,q_{u_r}})^2 + (y_l)^2}\right)/c, \tag{5}$$

For the convenience of analysis in the following context, let $\delta_{m_{u_t},l}^T$ be the path difference between the $m_{u_t}^{\text{th}}$ antenna and the target and the $M_T/2^{\text{th}}$ transmit antenna and the target, and $\delta_{q,l}^R$ be the path differences between the $q_{u_r}^{\text{th}}$ antenna and the target and the $Q_R/2^{\text{th}}$ receive antenna and the target, i.e.,

$$\delta_{m_{u_t},l}^T = \sqrt{(x_l - x_{T,m_{u_t}})^2 + (y_l)^2} - \rho_{M_T/2,l}^T, \tag{6}$$

$$\delta_{q_{u_r},l}^R = \sqrt{(x_l - x_{R,q_{u_r}})^2 + (y_l)^2} - \rho_{Q_R/2,l}^R, \tag{7}$$

where

$$\rho_{M_T/2,l}^T = \sqrt{(x_l - x_{T,M_T/2})^2 + (y_l)^2}, \tag{8}$$

$$\rho_{Q_R/2,l}^R = \sqrt{(x_l - x_{R,Q_R/2})^2 + (y_l)^2}. \tag{9}$$

On the other hand, let

$$\tau_{M_T/2,Q_R/2,l} = (\rho_{M_T/2,l}^T + \rho_{Q_R/2,l}^R)/c. \tag{10}$$

The expression in Eq. (5) can then be rewritten as

$$\tau_{m_{u_t},q_{u_r},l} = \tau_{M_T/2,Q_R/2,l} + (\delta_{m_{u_t},l}^T + \delta_{q_{u_r},l}^R)/c. \tag{11}$$

Furthermore, by sampling the waveform in Eq. (4) and by removing the guard interval at the receiver, the resulting signal at time $i\frac{T}{N}$ of the pth OFDM symbol is

$$y_{m_{u_t},q_{u_r},p}(i) = y_{m_{u_t},q_{u_r}}(t)|_{t=pT_0+T_{cp}+iT/N} \tag{12}$$

$$= \sum_{l=1}^{L} \sum_{n=0}^{N-1} \alpha_l \tilde{s}_{m_{u_t},n,p} e^{-j2\pi f_c(\tau_{M_T/2,Q_R/2,l} + \frac{\delta_{q_{u_r},l}^R + \delta_{m_{u_t},l}^T}{c})} e^{j2\pi(\frac{2v_{m_{u_t},q_{u_r},l} f_c}{c})(pT_0+iT/N-\tau_{m_{u_t},q_{u_r},l})}$$
$$e^{j2\pi(n+Km_{u_t})\Delta f(iT/N-\tau_{M_T/2,Q_R/2,l}-\frac{\delta_{q_{u_r},l}^R+\delta_{m_{u_t},l}^T}{c})} + z_{m_{u_t},q_{u_r},p}(i), i = 0, \ldots, N-1. \tag{13}$$

To simplify the analysis, we make the following assumptions.

A1 The antenna aperture D_T+D_R is small enough compared with $\frac{c}{N\Delta f}$ (Cohen et al., 2018). On the other

unedited

hand, because $\delta^R_{q_{u_r},l}+\delta^T_{m_{u_t},l}\le D_T+D_R$, it holds true that

$$N\Delta f\frac{\delta^R_{q_{u_r},l}+\delta^T_{m_{u_t},l}}{c}\ll 1. \tag{14}$$

Therefore, the effect of $e^{j2\pi n\Delta f\frac{\delta^R_{q_{u_r},l}+\delta^T_{m_{u_t},l}}{c}}$ in Eq. (13) can be ignored.

A2 The propagation time delay is small enough compared with the symbol duration T_0 (Gaudio et al., 2019), i.e.,

$$\tau_{m_{u_t},q_{u_r},l}\ll T_0. \tag{15}$$

Therefore, the term $e^{-j2\pi\frac{2v_{m_{u_t},q_{u_r},l}f_c\tau_{m_{u_t},q_{u_r},l}}{c}}$ in Eq. (13) can be ignored.

A3 The speed of the targets relative to the same subarray antenna is roughly equal, i.e.,

$$v_{m_{u_t},q_{u_r},l}\approx v_l^{u_t,u_r}. \tag{16}$$

This simplifies our signal model and subsequent parameter estimation process.

As a result of assumptions **A1**–**A3**, the expression in Eq. (13) can be approximated as,

$$\begin{aligned}y_{m_{u_t},q_{u_r},p}(i)=&\sum_{l=1}^{L}\sum_{n=0}^{N-1}\alpha_l\tilde{s}_{m_{u_t},n,p}e^{-j2\pi f_c(\tau_{M_T/2,Q_R/2,l}+\frac{\delta^R_{q_{u_r},l}+\delta^T_{m_{u_t},l}}{c})}e^{j2\pi(\frac{2v_l^{u_t,u_r}f_c}{c})(pT_0+iT/N)}\\&e^{j2\pi(n+Km_{u_t})\Delta f(iT/N-\tau_{M_T/2,Q_R/2,l})}e^{-j2\pi Km_{u_t}(\frac{\delta^R_{q_{u_r},l}+\delta^T_{m_{u_t},l}}{c})}+z_{m_{u_t},q_{u_r},p}(i),i=0,\dots,N-1.\end{aligned} \tag{17}$$

Performing a discrete Fourier transform (DFT) on $y_{m_{u_t},q_{u_r},p}(i), i=0,\dots,N-1,$ we arrive at (Gaudio et al., 2019),

$$\begin{aligned}y_{m_{u_t},q_{u_r},p,n}=&\frac{1}{N}\sum_{i=0}^{N-1}y_{m_{u_t},q_{u_r},p}(i)e^{-j2\pi\frac{ni}{N}}\\\approx&\sum_{l=1}^{L}\beta_l e^{-j2\pi n\Delta f\tau_{M_T/2,Q_R/2,l}}e^{j2\pi f_c(\frac{2v_l^{u_t,u_r}pT_0}{c})}\gamma_{m_{u_t},q_{u_r},l}+z_{m_{u_t},q_{u_r},p,n},\end{aligned} \tag{18}$$

in which

$$\beta_l=\alpha_l e^{-j2\pi f_c\tau_{M_T/2,Q_R/2,l}}\tilde{s}_{m_{u_t},n,p}, \tag{19}$$

$$\gamma_{m_{u_t},q_{u_r},l}=e^{-j2\pi Km_{u_t}\Delta f\left(\tau_{M_T/2,Q_R/2,l}+\frac{\delta^T_{m_{u_t},l}}{c}+\frac{\delta^R_{q_{u_r},l}}{c}\right)}e^{-j2\pi f_c\left(\frac{\delta^T_{m_{u_t},l}}{c}+\frac{\delta^R_{q_{u_r},l}}{c}\right)}. \tag{20}$$

From Eq. (20), one can see that if the phase of $2\pi\frac{K\Delta f}{c}\delta^R_{q_{u_r},l}$ exceeds [−π, π], it will cause phase ambiguity, resulting in inaccurate estimation of $\delta^R_{q_{u_r},l}$. Otherwise, when the condition $-\pi\le 2\pi\frac{K\Delta f}{c}\delta^R_{q_{u_r},l}\le\pi$ is met, $\delta^R_{q_{u_r},l}$ can be solved without ambiguity. On the other hand, it holds true that $\delta^R_{q_{u_r},l}\le\frac{Q_R d}{2}$. The combination of the above two equations indicates that if $d\le\frac{c}{2Q_R\Delta fK}$, there is no ambiguity concerning the estimation of $\delta^R_{q_{u_r},l}$. In general, we have $\frac{c}{Q_R\Delta fK}\gg\frac{c}{f_c}=\lambda$; thus, shifting the ambiguity constraints from the conventional within-one-wavelength antenna spacing to the used signal bandwidth, and increasing the scanning range of the antennas resolves the position ambiguity issue.

Our objective is to estimate $\{(x_l, y_l)\}$, $\{(v_{x,l}, v_{y,l})\}$ from the noise-corrupted observations $\{y_{m_{u_t}}, q_{u_r}, p, n\}$. Due to the coupled characteristics of $\{(x_l, y_l)\}$ and $\{(v_{x,l}, v_{y,l})\}$ in the observed data, it is difficult to extract them from Eq. (18) directly. In the following context, we will first organize the observed samples $y_{m_{u_t}}, q_{u_r}, p, n$ as an incomplete structured third-order tensor. Then, the unknown parameters $\{(x_l, y_l)\}$ and $\{(v_{x,l}, v_{y,l})\}$ can be estimated by analyzing the factor matrices obtained from the CANDE-COMP/PARAFAC (CP) decomposition of this incomplete tensor.

3 Joint estimation of position and velocity based on CP decomposition

In this section, we propose the CP-NFL algorithm, based on tensor decomposition, to estimate parameters with high estimation accuracy. This algorithm mainly consists of three steps: tensor formulation, tensor decomposition, and parameter estimation. Each step is described in the following, and the computational complexity of the proposed CP-NFL algorithm is analyzed.

3.1 Tensor formulation and CP decomposition

Because the transmitter and the radar receiver in the considered system are co-located as one, it is reasonable to assume that the transmitted messages $\tilde{S}_{m_{u_t},n,p}$ are known at the radar receiver. We remove $\tilde{S}_{m_{u_t},n,p}$ from the observed data $y_{m_{u_t}}, q_{u_r}, p, n$ and arrive at $\tilde{y}_{m_{u_t}}, q_{u_r}, p, n=y_{m_{u_t}}, q_{u_r}, p, n$. This, combined with the Eq. (18), indicates that

$$\begin{aligned}&\tilde{y}_{m_{u_t},q_{u_r},p,n}=\sum_{l=1}^{L}\tilde{\beta}_l e^{-j2\pi n\Delta f\tau_{M_T/2,Q_R/2,l}}e^{j2\pi f_c(\frac{2v_l^{u_t,u_r}pT_0}{c})}\gamma_{m_{u_t},q_{u_r},l}+\tilde{z}_{m_{u_t},q_{u_r},p,n},\\&m_{u_t}\in((u_t-1)M,u_tM-1),u_t=1,\dots,U_T,\\&q_{u_r}\in((u_r-1)Q,u_rQ-1),u_r=1,\dots,U_R,\\&p=0,1,\cdots,P-1,\\&n=0,1,\cdots,N-1.\end{aligned} \tag{21}$$

where $\tilde{\beta}_l=\beta_l/\tilde{s}_{m_{u_t},n,p}$ and

unedited

$\tilde{z}_{m_{u_t},q_{u_r},p,n} = z_{m_{u_t},q_{u_r},p,n} / \tilde{s}_{m_{u_t},n,p}$.

To better illustrate our method, we first show how to construct the tensor using the noiseless item $\tilde{y}_{m_{u_t},q_{u_r},p,n}$, i.e., letting

$$\tilde{x}_{m_{u_t},q_{u_r},p,n} = \sum_{l=1}^{L} \tilde{\beta}_l e^{-j2\pi n \Delta f \tau_{M_T/2,Q_R/2,l}} e^{j2\pi f_c \left(\frac{2v_l^{u_t,u_r} p T_0}{c}\right)} \gamma_{m_{u_t},q_{u_r},l}. \tag{22}$$

To obtain a tensor that admits a CP decomposition, let

$$\tilde{m}_{u_t,u_r} = (m_{u_t} - (u_t - 1)M)\,Q + q_{u_r} - (u_r - 1)Q,$$

and rearrange $\gamma_{m_{u_t},q_{u_r},l}$ to form $\gamma_{\tilde{m}_{u_t,u_r},l}$. Moreover, samples $\tilde{x}_{m_{u_t},q_{u_r},p,n}$ are rearranged to form a third-order tensor $\mathcal{X}_{u_t,u_r} \in \mathbb{C}^{N\times P\times MQ}$, whose three modes respectively stand for the sub-carrier, the OFDM symbol, and the transceiver antenna pairs, i.e.,

$$\mathcal{X}_{u_t,u_r} = \sum_{l=1}^{L} \tilde{\beta}_l \boldsymbol{a}_{u_t,u_r,l} \circ \boldsymbol{b}_{u_t,u_r,l} \circ \boldsymbol{c}_{u_t,u_r,l}, \tag{23}$$

where

$$\boldsymbol{a}_{u_t,u_r,l}(n) = e^{-j2\pi n \Delta f \tau_{M_T/2,Q_R/2,l}}, n = 0,1,\cdots,N-1, \tag{24}$$

$$\boldsymbol{b}_{u_t,u_r,l}(p) = e^{j2\pi f_c \left(\frac{2v_l^{u_t,u_r} p T_0}{c}\right)}, p = 0,1,\cdots,P-1, \tag{25}$$

$$\boldsymbol{c}_{u_t,u_r,l}(\tilde{m}_{u_t,u_r}) = \gamma_{\tilde{m}_{u_t,u_r},l}, \tilde{m}_{u_t,u_r} = 0,1,\cdots,MQ. \tag{26}$$

When only the observations $\{\tilde{y}_{m_{u_t}}, q_{u_r}, p, n\}$ are available, we can readily construct an incomplete third-order tensor $\mathcal{Y}_{u_t,u_r}$ using the manner in which $\mathcal{X}_{u_t,u_r}$ is constructed. Because the number of targets L is known a priori, the CP decomposition of $\mathcal{Y}_{u_t,u_r}$ can be accomplished by solving the following optimization problem:

$$\begin{aligned} &\min_{\hat{\boldsymbol{a}}_{u_t,u_r,l},\hat{\boldsymbol{b}}_{u_t,u_r,l},\hat{\boldsymbol{c}}_{u_t,u_r,l}} \|\mathcal{Y}_{u_t,u_r} - \mathcal{X}_{u_t,u_r}\|_F^2 \\ \Leftrightarrow &\min_{\hat{\boldsymbol{a}}_{u_t,u_r,l},\hat{\boldsymbol{b}}_{u_t,u_r,l},\hat{\boldsymbol{c}}_{u_t,u_r,l}} \left\| \mathcal{Y}_{u_t,u_r} - \sum_{l=1}^{L} \tilde{\beta}_l \boldsymbol{a}_{u_t,u_r,l} \circ \boldsymbol{b}_{u_t,u_r,l} \circ \boldsymbol{c}_{u_t,u_r,l} \right\|_F^2 \end{aligned} \tag{27}$$

According to Chen HY et al. (2021) and Li et al. (2023), we have the conclusions in the following lemma.

Lemma 1: Let $\boldsymbol{A} \in \mathbb{C}^{I_1\times I_2\times\cdots\times I_M}$ denote an Mth order tensor with its $(i_1, i_2, \ldots, i_M)$th entry denoted as $\mathcal{A}_{i_1,\cdots,i_M}$. Here, the order M of a tensor is the number of dimensions. The CP decomposition decomposes a tensor into a sum of rank-one component tensors, i.e.,

$$\mathcal{A} = \sum_{l=1}^{L_0} \boldsymbol{x}_l^1 \circ \boldsymbol{x}_l^2 \circ \cdots \circ \boldsymbol{x}_l^M,$$

where $\boldsymbol{x}_l^m \in \mathbb{C}^{I_m}$, $m \in (1,\ldots,M)$. The minimum achievable L_0 is referred to as the rank of the tensor, and $\boldsymbol{X}^m = [\boldsymbol{x}_1^m, \cdots, \boldsymbol{x}_{L_0}^m] \in \mathbb{C}^{I_m\times L_0}$ denotes the factor along the mth mode. When the Kruskal Condition holds true, i.e.,

$$\min(I_1, L_0) + \min(I_2, L_0) + \cdots + \min(I_M, L_0) \geq 2L_0 + 2,$$

the CP decomposition is unique.

Applying the above **Lemma** 1 to Eq. (27), one can see that the tensor $\mathcal{Y}_{u_t,u_r} \in \mathbb{C}^{N\times P\times MQ}$ can be decomposed into a sum of rank-one component tensors

$$\hat{\boldsymbol{a}}_{u_t,u_r,l}, \hat{\boldsymbol{b}}_{u_t,u_r,l}, \hat{\boldsymbol{c}}_{u_t,u_r,l}, l = 1,\cdots,L, u_t = 1,\cdots,U_T, u_r = 1,\cdots,U_R.$$

Moreover, because in general, the number of OFDM symbols P, the number of sub-carriers N, and the number of antennas MQ is greater than the number of targets L, the Kruskal Condition holds true because the number of targets $L\geq 2$. On the other hand, the work in De Lathauwer (2006) demonstrates that for the case $L=1$, the CP decomposition also holds true. Therefore, as long as the number of OFDM symbols P, the number of sub-carriers N, and the number of antennas MQ is greater than the number of targets L, the above CP decomposition given by **Lemma 1** is unique.

3.2 Parameter estimation

We now discuss how to estimate the parameters $\{(x_l, y_l)\}$ and $\{(v_{x,l}, v_{y,l})\}$ based on the estimated factor matrices composed of $\hat{\boldsymbol{a}}_{u_t,u_r,l}, \hat{\boldsymbol{b}}_{u_t,u_r,l}, \hat{\boldsymbol{c}}_{u_t,u_r,l}$.

Considering Eq. (24), one can see that $\boldsymbol{a}_{u_t,u_r,l}$ is characterized by the associated propagation time delay of $\tau_{M_T/2,Q_R/2,l}$. Hence, the associated propagation time delay of $\tau_{M_T/2,Q_R/2,l}$ can be estimated via reformulating Eq. (24) and utilizing a simple averaging method over the sub-carrier index n, yielding

$$\hat{\tau}_{M_T/2,Q_R/2,l} = \frac{1}{2\pi\Delta f(N-1)U_T U_R} \sum_{u_t=1}^{U_T}\sum_{u_r=1}^{U_R}\sum_{n=0}^{N-2} \angle\left(\frac{\hat{\boldsymbol{a}}_{u_t,u_r,l}(n)}{\hat{\boldsymbol{a}}_{u_t,u_r,l}(n+1)}\right). \tag{28}$$

Similarly, by considering Eq. (25), one can see that $\boldsymbol{b}_{u_t,u_r,l}$ is characterized by the associated propagation length $v_l^{u_t,u_r}$, which can be estimated by reformulating Eq. (25) and using a simple averaging method over the OFDM symbol index p, yielding

$$\hat{v}_l^{u_t,u_r} = \frac{c}{4\pi f_c T_0(P-1)} \sum_p \angle\left(\frac{\hat{\boldsymbol{b}}_{u_t,u_r,l}(p)}{\hat{\boldsymbol{b}}_{u_t,u_r,l}(p+1)}\right). \tag{29}$$

unedited

By considering Eqs. (26) and (20), one can see that $\boldsymbol{c}_{u_t,u_r,l}$ is characterized by the associated propagation length difference $\delta^R_{q_{u_r},l}$, which can be estimated by combining Eqs. (26) and (20), and using a simple averaging method over $\tilde{m}_{u_t,u_r}$, yielding

$$\hat{\delta}^R_{q_{u_r},l} = \frac{c}{2\pi K \Delta f M_T} \sum_{u_t=1}^{U_T} \sum_{m_{u_t}=1}^{M} \angle\left(\frac{\hat{\gamma}_{m_{u_t},q_{u_r},l}}{\hat{\gamma}_{m_{u_t},Q_R/2,l}} \Big/ \frac{\hat{\gamma}_{m_{u_t}-1,q_{u_r},l}}{\hat{\gamma}_{m_{u_t}-1,Q_R/2,l}}\right). \tag{30}$$

where by definition it holds true that $\hat{\gamma}_{m_{u_t},q_{u_r},l} = \hat{\boldsymbol{c}}_{u_t,u_r,l}(\tilde{m}_{u_t,u_r})$.

3.2.1 Estimation of $\{(x_l, y_l)\}$

By the definition of $\delta^R_{q_{u_r},l}$ and $\tau_{M_T/2,Q_R/2,l}$ in Eqs. (7) and (10), respectively, one can see that these parameters are related to $\{x_l, y_l\}$. Inspired by these observations, in the following, we focus on solving $\{x_l, y_l\}$ from Eqs. (7) and (10).

By re-arranging the formulas in Eq. (7), we arrive at

$$\left(\delta^R_{q_{u_r},l} + \rho^R_{Q_R/2,l}\right)^2 = (x_l)^2 + (y_l)^2 + \left(x_{R,q_{u_r}}\right)^2 - 2x_{R,q_{u_r}} x_l, \tag{31}$$

which, combined with Eq. (9), indicates that

$$2(x_{R,q_{u_r}} - x_{R,Q_R/2})x_l + 2\delta^R_{q_{u_r},l}\rho^R_{Q_R/2,l} = (x_{R,q_{u_r}})^2 - (x_{R,Q_R/2})^2 - (\delta^R_{q_{u_r},l})^2. \tag{32}$$

where

$$q_{u_r} \in ((u_r-1)Q, u_rQ-1),\ u_t \in (1,\ldots,U_T).$$

Therefore, we have several Q_R equations based on Eq. (32). Reformulating those equations as a vector, we have

$$\mathbf{P}\boldsymbol{w}_l = \boldsymbol{h}_l. \tag{33}$$

where

$$\mathbf{P} \triangleq 2\begin{bmatrix} x_{R,0} - x_{R,Q_R/2} & \delta^R_{0,l} \\ x_{R,1} - x_{R,Q_R/2} & \delta^R_{1,l} \\ \vdots & \vdots \\ x_{R,Q_R-1} - x_{R,Q_R/2} & \delta^R_{Q_R-1,l} \end{bmatrix}, \boldsymbol{w}_l \triangleq \begin{bmatrix} x_l \\ \rho^R_{Q_R/2,l} \end{bmatrix},$$

$$\boldsymbol{h}_l \triangleq \begin{bmatrix} (x_{R,0})^2 - (x_{R,Q_R/2})^2 - \left(\delta^R_{0,l}\right)^2 \\ (x_{R,1})^2 - (x_{R,Q_R/2})^2 - \left(\delta^R_{1,l}\right)^2 \\ \vdots \\ (x_{R,Q_R-1})^2 - (x_{R,Q_R/2})^2 - \left(\delta^R_{Q_R-1,l}\right)^2 \end{bmatrix}. \tag{34}$$

On the other hand, the combination of Eqs. (8) and (9) indicates that

$$\rho^T_{M_T/2,l} = \sqrt{(\rho^R_{Q_R/2,l})^2 + 2x_l(x_{R,Q_R/2} - x_{T,M_T/2})}. \tag{35}$$

Substituting $\rho^T_{M_T/2,l}$ in Eq. (35) into Eq. (10), we obtain

$$\rho^R_{Q_R/2,l} + \sqrt{(\rho^R_{Q_R/2,l})^2 + 2\xi x_l} = c\tau_{M_T/2,Q_R/2,l}, \tag{36}$$

where $\xi \triangleq x_{R,Q_R/2} - x_{T,M_T/2}$.

If the estimations of $\delta^r_{q,l}$ and $\tilde{\tau}_{M_T/2,Q_R/2,l}$ are perfect, substituting them into Eqs. (33) and (36) and solving the resulting equations, we can obtain the variables x_l and $\rho^R_{Q_R/2,l}$. However, due to the estimation error of $\hat{\delta}^r_{q,l}$ and $\tilde{\tau}_{M_T/2,Q_R/2,l}$, the resulting equations may not hold true. As such, we optimize the following square error with respect to x_l and $\rho^R_{Q_R/2,l}$.

$$\begin{aligned} &\min_{\hat{x}_l,\hat{\rho}^R_{Q_R/2,l}} \left\|\hat{\mathbf{P}}\boldsymbol{w}_l - \hat{\boldsymbol{h}}_l\right\|_F^2 + \left|c\hat{\tau}_{M_T/2,Q_R/2,l} - \sqrt{(\rho^R_{Q_R/2,l})^2 + 2\xi x_l} - \rho^R_{Q_R/2,l}\right|^2 \\ &s.t.\ \rho^R_{Q_R/2,l} \geq \left|x_l - x_{R,Q_R/2}\right|. \end{aligned} \tag{37}$$

where $\hat{\boldsymbol{P}}$ and $\hat{\boldsymbol{h}}_l$ are obtained by substituting $\hat{\delta}^r_{q,l}$ and $\tilde{\tau}_{M_T/2,Q_R/2,l}$ into Eqs. (33) and (36), respectively.

The above optimization problem is non-convex due to the nonlinear item $\sqrt{(\rho^R_{Q_R/2,l})^2 + 2\xi x_l}$. In the following, our key approach for solving this problem is to perform Taylor expansion on that item, by which we convert the optimization problem into a convex one. To that end, we first need to know a rough estimation of x_l and $\rho^R_{Q_R/2,l}$, which is given by **Lemma** 2.

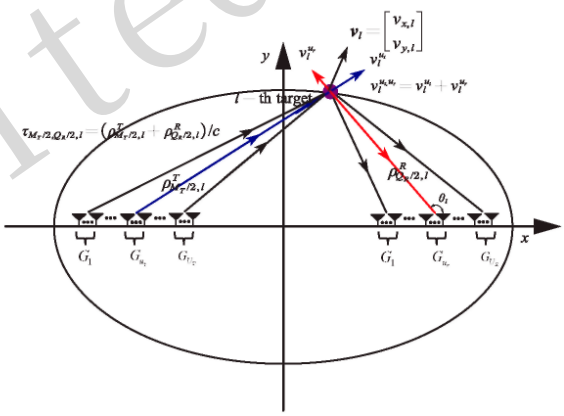

Fig. 2 Illustration of the rough estimation model. The target is located on an ellipse, which is determined by $\hat{\boldsymbol{\tau}}_l$, and the two focal points of the ellipse are the $M_T/2^{\text{th}}$ transmitting antenna and the $Q_R/2^{\text{th}}$ receiving antenna. The position of the target is at the intersection of the ellipse and the azimuth θ_l

Lemma 2: Let θ_l be the azimuth of the target relative to the $Q_R/2^{\text{th}}$ receiving antenna, as shown in Fig. 2. Combining Eqs. (33) and (36), we arrive at

$$\breve{\rho}^R_{Q_R/2,l} = \frac{\left(c\hat{\tau}_{M_T/2,Q_R/2,l}\right)^2 + 2\xi^2}{2c\hat{\tau}_{M_T/2,Q_R/2,l} - 2\cos\hat{\theta}_l\xi},$$

$$\breve{x}_l = \breve{\rho}^R_{Q_R/2,l}\cos\left(\hat{\theta}_l\right) + x_{R,Q_R/2},$$

The proof is given in Appendix A.

Performing a Taylor expansion of $\sqrt{(\rho^R_{Q_R/2,l})^2 + 2\xi x_l}$ near the point $\breve{x}_l, \breve{\rho}^R_{Q_R/2,l}$, we

unedited

obtain

$$\begin{aligned}&\sqrt{(\rho^R_{Q_R/2,l})^2+2\xi x_l}\\&=\sqrt{(\breve{\rho}^R_{Q_R/2,l})^2+2\breve{x}_l\xi}+\frac{\breve{\rho}^R_{Q_R/2,l}}{\sqrt{(\breve{\rho}^R_{Q_R/2,l})^2+2\breve{x}_l\xi}}\left(\rho^R_{Q_R/2,l}-\breve{\rho}^R_{Q_R/2,l}\right)+\frac{\xi}{\sqrt{(\breve{\rho}^R_{Q_R/2,l})^2+2\breve{x}_l\xi}}(x_l-\breve{x}_l).\end{aligned} \tag{38}$$

On the other hand, substituting $\breve{x}_l$ and $\breve{\rho}^R_{Q_R/2,l}$ into Eq. (36), we obtain

$$\breve{\rho}^R_{Q_R/2,l}=c\hat{\tau}_{M_T/2,Q_R/2,l}-\sqrt{(\breve{\rho}^R_{Q_R/2,l})^2+2\breve{x}_l\xi}. \tag{39}$$

The combination of Eqs. (38) and (39), yields

$$\begin{aligned}&\left|c\hat{\tau}_{M_T/2,Q_R/2,l}-\sqrt{(\breve{\rho}^R_{Q_R/2,l})^2+2x_l\xi}-\rho^R_{Q_R/2,l}\right|^2\\&=\left|\begin{array}{l}\breve{\rho}^R_{Q_R/2,l}-\frac{\breve{\rho}^R_{Q_R/2,l}}{\sqrt{(\breve{\rho}^R_{Q_R/2,l})^2+2\breve{x}_l\xi}}\left(\rho^R_{Q_R/2,l}-\breve{\rho}^R_{Q_R/2,l}\right)\\-\frac{\breve{x}_l\xi}{\sqrt{(\breve{\rho}^R_{Q_R/2,l})^2+2\breve{x}_l\xi}}(x_l-\breve{x}_l)-\rho^R_{Q_R/2,l}\end{array}\right|^2\\&=\left|\begin{array}{l}\breve{\rho}^R_{Q_R/2,l}+\frac{(\breve{\rho}^R_{Q_R/2,l})^2+\breve{x}_l^2\xi}{\sqrt{(\breve{\rho}^R_{Q_R/2,l})^2+2\breve{x}_l\xi}}-\left(1+\frac{\breve{\rho}^R_{Q_R/2,l}}{\sqrt{(\breve{\rho}^R_{Q_R/2,l})^2+2\breve{x}_l\xi}}\right)\rho^R_{Q_R/2,l}\\-\frac{\breve{x}_l\xi}{\sqrt{(\breve{\rho}^R_{Q_R/2,l})^2+2\breve{x}_l\xi}}x_l\end{array}\right|^2.\end{aligned} \tag{40}$$

Substituting Eq. (40) into the optimization problem Eq. (37) and reformulating, we can convert Eq. (37) to a convex optimization problem as follows

$$\begin{aligned}&\min_{\hat{x}_l,\hat{\rho}^R_{Q_R/2,l}}\ \|\mathbf{P}'\boldsymbol{w}_l-\mathbf{h}'_l\|^2\\&s.t.\ \rho^R_{Q_R/2,l}\geq\left|x_l-x_{R,Q_R/2}\right|\end{aligned} \tag{41}$$

where

$$\mathbf{P}'=\begin{bmatrix}\hat{\mathbf{P}} & \\ \frac{\breve{x}_l\xi}{\sqrt{(\breve{\rho}^R_{Q_R/2,l})^2+2\breve{x}_l\xi}} & \left(1+\frac{\breve{\rho}^R_{Q_R/2,l}}{\sqrt{(\breve{\rho}^R_{Q_R/2,l})^2+2\breve{x}_l\xi}}\right)\end{bmatrix},\ \mathbf{h}'_l=\begin{bmatrix}\hat{\boldsymbol{h}}_l\\ \breve{\rho}^R_{Q_R/2,l}+\frac{(\breve{\rho}^R_{Q_R/2,l})^2+\breve{x}_l^2\xi}{\sqrt{(\breve{\rho}^R_{Q_R/2,l})^2+2\breve{x}_l\xi}}\end{bmatrix}.$$

The optimization problem in Eq. (41) is convex, where $\hat{x}_l$ and $\hat{\rho}^R_{Q_R/2,l}$ can be obtained using the CVX toolbox. Substituting $\hat{x}_l$ and $\hat{\rho}^R_{Q_R/2,l}$ into Eq. (9), we get

$$\hat{y}_l=\sqrt{(\hat{\rho}^R_{Q_R/2,l})^2-(\hat{x}_l-x_{R,Q_R/2})^2}, \tag{42}$$

This completes the estimation of $\{(x_l, y_l)\}$.

3.2.2 Estimation of $\{(v_{x,l}, v_{y,l})\}$

In the near field and by definition, the observed velocity is different for different groups of transceiver antennas, and is estimated in Eq. (29). Obviously, this observed velocity is related not only to the target's velocity $\{(v_{x,l}, v_{y,l})\}$ but also to the target's position (x_l, y_l). In this section, we give details for obtaining $\{(v_{x,l}, v_{y,l})\}$ based on $\hat{v}_l^{u_t,u_r}$ and $\{(\hat{x}_l,\hat{y}_l)\}$.

As shown in Fig. 2, the velocity $v_l^{u_t,u_r}$ consists of two parts: $v_l^{u_t,u_r}=v_l^{u_t}+v_l^{u_r}$, where $v_l^{u_t}$ and $v_l^{u_r}$ are the radial velocities relative to the transmitting and receiving sub-arrays, respectively. According to the geometric information, $v_l^{u_t}$ and $v_l^{u_r}$ can be rewritten as, respectively,

$$v_l^{u_t}=\frac{v_{x,l}(x_{T,(u_t-\frac{1}{2})M}-x_l)-v_{y,l}y_l}{\rho^T_{(u_t-\frac{1}{2})M,l}}, \tag{43}$$

$$v_l^{u_r}=\frac{v_{x,l}(x_{R,(u_r-\frac{1}{2})Q}-x_l)-v_{y,l}y_l}{\rho^R_{(u_r-\frac{1}{2})Q,l}}. \tag{44}$$

where $(x_{T,(u_t-\frac{1}{2})M},0)$ and $(x_{R,(u_r-\frac{1}{2})Q},0)$ are the location of the center antenna of the u_t^{th} transmit sub-array and u_r^{th} receive sub-array. Therefore, $v_l^{u_t,u_r}$ can be rewritten as

$$\begin{aligned}&v_l^{u_t,u_r}=\begin{bmatrix}\frac{x_{T,(u_t-\frac{1}{2})M}-x_l}{\rho^T_{(u_t-\frac{1}{2})M,l}}+\frac{x_{R,(u_r-\frac{1}{2})Q}-x_l}{\rho^R_{(u_r-\frac{1}{2})Q,l}} & \frac{-y_l}{\rho^T_{(u_t-\frac{1}{2})M,l}}+\frac{-y_l}{\rho^R_{(u_r-\frac{1}{2})Q,l}}\end{bmatrix}\begin{bmatrix}v_{x,l}\\v_{y,l}\end{bmatrix},\\&u_t=1,\ldots,U_T,u_r=1,\ldots,U_R.\end{aligned} \tag{45}$$

Let $\hat{\boldsymbol{v}}_l\triangleq\left[\hat{v}_l^{1,1},\cdots\hat{v}_l^{U_T,U_R}\right]^T$, where $\hat{v}_l^{u_t,u_r},u_t=1,\ldots,U_T,u_r=1,\ldots,U_R$ are obtained using Eq. (29). Substituting the estimated velocity of $\hat{v}_l^{u_t,u_r}$ and the position $(\hat{x}_l,\hat{y}_l)$ into Eq. (45), we obtain several U_TU_R equations, which can be re-written as

$$\hat{\boldsymbol{v}}_l=\boldsymbol{G}\begin{bmatrix}\hat{v}_{x,l}\\\hat{v}_{y,l}\end{bmatrix}. \tag{46}$$

where

$$\boldsymbol{G}\triangleq\begin{bmatrix}\frac{x_{T,\frac{M}{2}}-\hat{x}_l}{\rho^T_{\frac{M}{2},L}}+\frac{x_{R,\frac{Q}{2}}-\hat{x}_l}{\rho^R_{\frac{Q}{2},l}} & \frac{-\hat{y}_l}{\rho^T_{\frac{M}{2},L}}+\frac{-\hat{y}_l}{\rho^R_{\frac{Q}{2},l}}\\ \vdots & \vdots\\ \frac{x_{T,(U_T-\frac{1}{2})M}-\hat{x}_l}{\rho^T_{(U_T-\frac{1}{2})M,l}}+\frac{x_{R,(U_T-\frac{1}{2})Q}-\hat{x}_l}{\rho^R_{(U_R-\frac{1}{2})Q,l}} & \frac{-\hat{y}_l}{\rho^T_{(U_T-\frac{1}{2})M,l}}+\frac{-\hat{y}_l}{\rho^R_{(U_R-\frac{1}{2})Q,l}}\end{bmatrix}.$$

Finally, $\hat{v}_{x,l}$ and $\hat{v}_{y,l}$ can be estimated by the least squares (LS) algorithm

$$\begin{bmatrix}\hat{v}_{x,l}\\\hat{v}_{y,l}\end{bmatrix}=\left(\boldsymbol{G}^T\boldsymbol{G}\right)^{-1}\boldsymbol{G}^T\hat{\boldsymbol{v}}_l. \tag{47}$$

The algorithm discussed above provides a method of target localization and velocity estimation based on the estimated parameters at tensor decomposition. To improve the localization accuracy, an optimization problem is constructed by combining parameters $\hat{\tau}_{M_T/2,Q_R/2,l}$ and $\hat{\delta}^R_{q_{u_r},l}$ under the minimum variance criterion. Then, the target velocity is estimated by using the estimated target position and $\hat{v}_l^{u_t,u_r}$. To summarize, the proposed CP-NFL algorithm is presented as Algorithm 1 as follows.

Algorithm 1 CP-NFL Algorithm

Inputs: array groupings U_T and U_R, tensors of receiving data $\mathcal{Y}_1,\mathcal{Y}_2\cdots\mathcal{Y}_{U_RU_T}$, target number L;

unedited

Output: position $(\hat{x}_l, \hat{y}_l)$, velocity $(\hat{v}_{x,l}, \hat{v}_{y,l})$, $\forall l \in (1, \ldots, L)$;

1: **for** $u_t = 1$: U_T **do**

2: **for** $u_r = 1$: U_R **do**

3: Tensor decomposition of $\mathcal{Y}_{u_t u_r}$

4: Yielding $\hat{\boldsymbol{a}}_{u_t,u_r,l}, \hat{\boldsymbol{b}}_{u_t,u_r,l}, \hat{\boldsymbol{c}}_{u_t,u_r,l}$.

5: **end for**

6: **end for**

7: **for** $l = 1$: L **do**

8: Compute $\hat{\tau}_{M_T/2,Q_R/2,l}, \hat{v}_l^{u_t,u_r}$ and $\hat{\delta}^R_{q_{u_r},l}$ using Eqs. (28)–(30), respectively.

9: Compute $\breve{x}_l$ and $\breve{\rho}^R_{Q_R/2,l}$ by **Lemma 2**.

10: Estimate $\left(\hat{x}_l, \hat{\rho}^R_{Q_R/2,l}\right)$ by solving the optimization problem Eq. (41) with the CVX tool.

11: Compute the position parameter $\hat{x}_l$ using Eq. (42).

12: Compute the velocity $(\hat{v}_{x,l}, \hat{v}_{y,l})$ using Eq. (47).

13: **end for**

3.3 Computational complexity analysis

The computational complexity of the significant steps of the CP-NFL algorithm include CP decomposition, estimation of $\hat{\tau}_{M_T/2,Q_R/2,l}, \hat{v}_l^{u_t,u_r}, \hat{\delta}^R_{q_{u_r},l}$, and solving the optimization problem in Eq. (45). The computational complexity of tensor decomposition for each group of received data is (da Rosa Zanatta et al., 2019):

$$\mathcal{O}(CPD) = \mathcal{O}\left(P^3 + N^3 + (MQ)^3 + L^3 + LMQN^2 + L(MQ)^2N + L^2PNMQ\right).$$

The computational complexity of estimating $\hat{\tau}_{M_T/2,Q_R/2,l}, \hat{v}_l^{u_t,u_r}, \hat{\delta}^R_{q_{u_r},l}$ is O(LMQ) for each group. The computational complexity of localization by solving the optimization problem is $O(T)$ where T is the number of iterations. Because there are U_TU_R groups, the total computational complexity is U_TU_R (O (CPD) + O (LMQ)) + $O(T)$. Meanwhile, O (LMQ) can be ignored when it is compared to O (CPD). Finally, we can obtain

$$\begin{aligned}\mathcal{O}(CP-NFL) &= U_TU_R(\mathcal{O}(CPD)) + \mathcal{O}(T) \\ &= \mathcal{O}\left(U_TU_R(P^3 + N^3 + L^3) + \frac{(M_TQ_R)^3}{(U_TU_R)^2} + L\frac{(M_TQ_R)^2}{U_TU_R}N\right) \\ &\quad + \mathcal{O}(LM_TQ_RN^2 + L^2PNM_TQ_R) + \mathcal{O}(T).\end{aligned} \tag{48}$$

As we can see, the computational complexity varies with the number of groups. When M_TQ_R is larger than Q, P, and N, appropriately increasing the number of groups can reduce the complexity caused by the number of antennas, and thus reduce the overall complexity.

4 Numerical results

This section presents numerical results to validate the proposed schemes. In the simulation, we set the carrier frequency to f_c = 300 GHz, which results in the wavelength $\lambda = c/f_c$ = 1 mm, and the subcarrier spacing to Δf = 300 kHz, so the OFDM symbol duration in this case is $T_0 = 1/\Delta f + T_{\mathrm{CP}}$ = $1.25/\Delta f \approx 4.1667$ us. The distance between the origin of the coordinate and 0th transmit or receive antenna is d' = 0.2 m, and the antenna element spacing is set to $d = 10\lambda$ = 1 cm, thus, the total size of the receiving array is $D_r = Q_Rd$ = 0.3 m. Assume that the parameter estimation is carried out over a frame of P = 60 OFDM symbols, and let the integer K = 401. We assume that the target is located in the area with $\theta \in [-90°, 90°]$ in elevation and $r \in [1\text{ m}, 30\text{ m}]$ in distance. All simulations were performed with K_T = 1,000 trials. Unless otherwise specified, the number of receiving antennas is Q_R = 30, which is divided into six groups (U_R = 6), and the number of transmitting antennas is M_T = 31, which constitutes one group (U_T = 1). The velocity is defined in polar coordinates. Unless otherwise specified, the angle of the velocity is set as 45°. In the scenario with one target, the magnitude of its velocity is set as 0.5 m/s; therefore, the magnitude along the cartesian coordinates are $v_x = 0.5/\sqrt{2}$ m/s and $v_y = 0.5/\sqrt{2}$ m/s, respectively. For the scenario with two targets, the magnitude of their velocities are set as 0.5 m/s and 0.7 m/s, respectively. Meanwhile, the signal noise ratio (SNR), the root mean square error (RMSE) of localization, and the RMSE of velocity in this study are defined as, respectively,

$$SNR = \frac{P_t}{L\sigma^2}\sum_l |\alpha_l|^2, \tag{49}$$

$$RMSE_{xy} = \mathbb{E}\left(\sum_l \frac{\sqrt{(x_l - \hat{x}_l)^2 + (y_l - \hat{y}_l)^2}}{2L}\right), \tag{50}$$

$$RMSE_v = \mathbb{E}\left(\sum_l \frac{\sqrt{(\hat{v}_{x,l} - v_{x,l})^2 + (\hat{v}_{y,l} - v_{y,l})^2}}{2L}\right), \tag{51}$$

where α_l represents the path loss from the transmit antenna to the receive antenna related to the lth target. P_t denotes the transmit power and σ^2 denotes variance of noise. $\mathbb{E}(\bullet)$ represents averaging. In addition, the

unedited

bandwidth in the simulation refers to the signal bandwidth of each transmitting antenna and the bandwidth is set to 120 MHz if it is not specified.

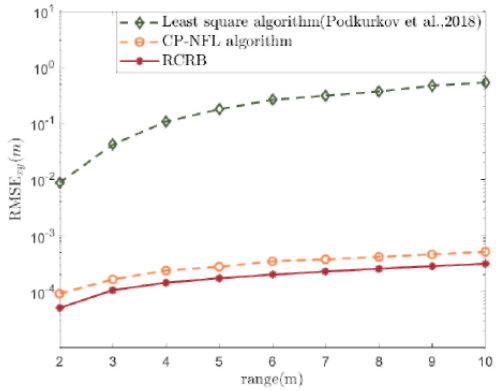

Fig. 3 The RMSE of localization w.r.t. range (distance from target to origin) when the SNR is 15 dB. CP-NFL, CP decomposition Near-Field Localization

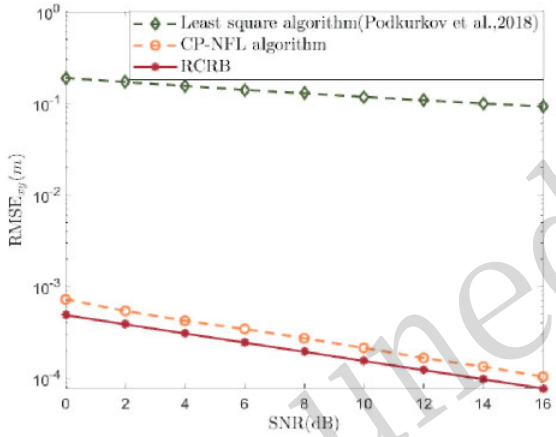

Fig. 4 The RMSE of localization w.r.t. SNR. CP-NFL, CP decomposition Near-Field Localization

Figs. 3 and 4 show the relationships between the RMSE, distance from target to origin, and SNR of the proposed CP-NFL algorithm. The CP-NFL algorithm is compared with the near-field LS localization algorithm proposed in Podkurkov et al. (2018). From Fig. 3, one can see that the estimation performance of the proposed CP-NFL algorithm is much better than that of the LS algorithm. Overall, the accuracy of the algorithms decreases with increasing distance. However, due to the more delicate use of the signal model based on spherical wavefronts, the performance of the CP-NFL algorithm deteriorates more slowly than that of the LS algorithm. In Fig. 4, we set the target distance at 5 m. The figure shows that with increasing SNR, the estimation performance of both algorithms improves. Meanwhile, the estimation performance by the proposed CP-NFL algorithm is better and improves faster as compared with the existing LS algorithm.

In Fig. 5, two targets are considered. We set the distance from the first target to origin (r_1) as 10 m, 20 m, 30 m, and 200 m. The x-coordinate denotes the distance between the second target and the first target ($\Delta_d = r_2 - r_1$), where r_2 is the distance from the second target to the origin. It can be seen that the estimation accuracy increases as the distance to the first target r_1 decreases. The reason is that the near-field effect is more obvious when r_1 decreases. Moreover, it is more difficult to distinguish the two targets when the two targets are too close, and the estimation accuracy decreases as the distance between the two targets decreases. When Δ_d is >0.21 m, the estimation performance improves slightly with increasing Δ_d, and when Δ_d is >0.068 m, the estimation accuracy in the near-field scene can reach the centimeter level. This indicates that when the estimation performance of the CP-NFL algorithm is affected by Δ_d, the estimation accuracy achieves 0.01 m. In Fig. 6, we set the velocity of the two targets as 0.5 m/s and 0.7 m/s, respectively. Because the estimation accuracy of the velocity is affected by that of the position, the variation trend of its estimation accuracy is the same as that in Fig. 5.

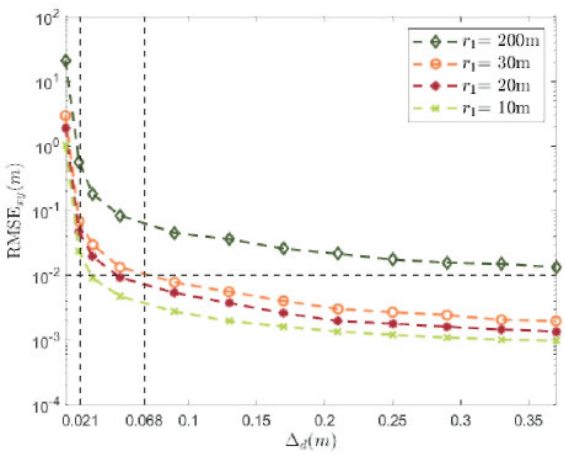

Fig. 5 The RMSE of localization w.r.t. the range between targets with different distances to the first target (SNR=15 dB)

unedited

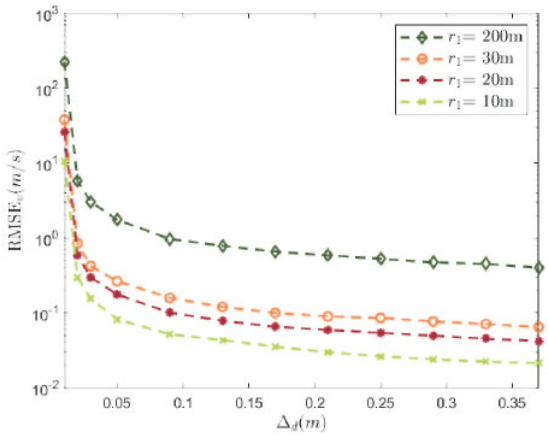

Fig. 6 The RMSE of velocity w.r.t. the range between targets with different distances to the first target (SNR=15 dB)

In Figs. 7 and 8, we set r_1 = 10 m. The bandwidth varies from 15 MHz to 120 MHz. With the increase in available bandwidth, the estimation accuracy gradually improves, because in this case the estimation of the propagation time delay is more accurate. In addition, when the distance between two targets is >0.045 m and 0.225 m for the cases of 120 MHz and 30 MHz, respectively, the estimation accuracy of the proposed CP-NFL algorithm reaches millimeter levels, in which case we can differentiate the two targets. This trend is consistent with the well-known radar theory that as the bandwidth increases, the radar resolution increases. Specifically, by the radar equation, the range resolution is proportional to the bandwidth. Therefore, the range estimation accuracy gradually increases with increasing bandwidth, resulting in a more accurate estimation of the location information of the two targets. Moreover, the velocity estimation in Eq. (47) makes use of the estimated location information, so the accuracy of the velocity estimation also increases, which leads to improved velocity resolution.

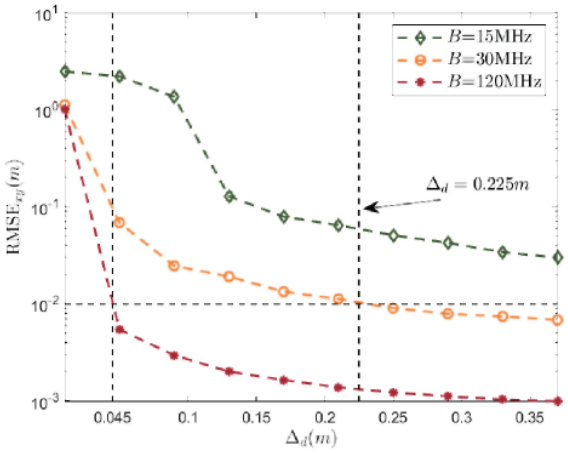

Fig. 7 RMSE of localization w.r.t. the range between targets with different bandwidths (SNR=15 dB)

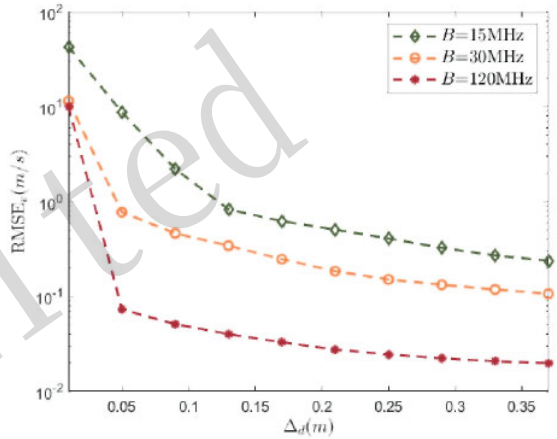

Fig. 8 The RMSE of velocity w.r.t. the range between targets with different signal bandwidths (SNR=15 dB)

Fig. 9 illustrates the achievable estimation accuracy with respect to the number of groups of sub-arrays at the receiver. The number of transmit antennas is set to $M_T = 3$, which is considered as one group ($U_T = 1$). The number of receive antennas is set to Q_R = 60. Fig. 9 shows that, as the number of sub-arrays increases, the estimation accuracy deteriorates, but this deterioration disappears because the SNR is >−4 dB, which is generally the operating case of a system. On the other hand, as analyzed in the Section 3.3, dividing the receive antennas into a larger number of groups reduces the computational complexity of the proposed algorithm. Therefore, it is necessary to make a reasonable choice between the algorithm complexity and the estimation accuracy. Fig. 9 shows that with increasing SNR, the number of groups has less influence on the estimation performance, and when SNR is high, it is preferable to divide the antennas into a larger number of groups.

unedited

Fig. 10 illustrates the effect of velocity on the algorithm. Specifically, the target velocity in the x and y directions is identical, that is, $v_x = v_y = v/\sqrt{2}$. This describes the achievable estimation accuracy with respect to the SNR under different velocity v, where the receiving antennas are divided into 6 groups. As the figure shows, with increasing velocity, the localization accuracy gradually deteriorates. According to Assumption A3 in Section 2, the velocity of the targets relative to the same sub-array antenna is roughly equal. As the velocity increases, Assumption A3 gradually loses validity, and the discrepancy between our signal model and the actual signal model grows, which leads to deterioration of localization performance.

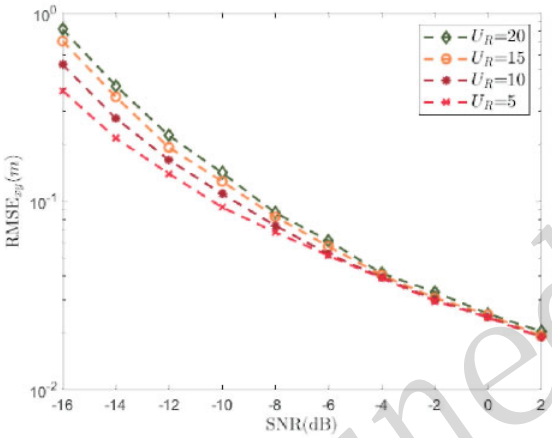

Fig. 9 RMSE of localization w.r.t. the SNR with different numbers of sub-array groups

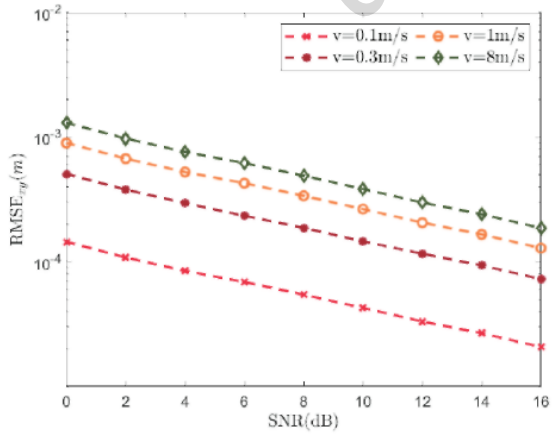

Fig. 10 RMSE of localization w.r.t. the SNR for different velocity cases

5 Conclusion

We proposed a CP decomposition-based method for the joint estimation of the position and velocity of multiple targets using a terahertz MIMO-OFDM system operating in the near-field region, where the waveforms transmitted from each antenna carry communication messages and are orthogonal to each in the frequency domain. The proposed CP-NFL method exploits the intrinsic multi-dimensional structure of the multi-channel received signal. Specifically, the received signal was expressed as a third-order tensor. We showed that the tensor has a low-rank CP decomposition form, and used the tensor's decomposed factor matrices to convert the original non-convex optimization problem into a convex one. The investigation of the CP decomposition uniqueness revealed that it can be guaranteed, even with a small number of targets. To further reduce the computational complexity of the proposed algorithm, we divided the antennas into several sub-arrays. Our analysis showed that the computational complexity of the proposed method is linear to the sum of the third power of the number of sub-carriers, OFDM symbols, antennas, and targets. We compared our proposed method with the existing LS-based parameter estimation method using simulations, and demonstrated the impact of systems parameters on the estimation accuracy, highlighting the advantage of the proposed CP-NFL method.

unedited

Appendix A

According to Eq. (33), x_l, $\rho^R_{M_R/2,\,l}$, can be directly obtained by the LS algorithm

$$\begin{bmatrix} \bar{x}_l \\ \bar{\rho}^R_{M_R/2,l} \end{bmatrix} = \left(\mathbf{P}^T\mathbf{P}\right)^{-1}\mathbf{P}^T\boldsymbol{h}_l. \tag{52}$$

However, previous studies (Podkurkov et al., 2018) indicate that the accuracy of range $\hat{\rho}^R_{Q_R/2,\,l}$ estimation decreases seriously as the distance to the target increases, which will cause deterioration of the localization performance. Fortunately, the estimation of θ_l (the azimuth of the target relative to the $Q_R/2^{\text{th}}$ receiving antenna, Fig. 2) is highly accurate (Podkurkov et al., 2018). Thus, we use $\hat{x}_l$ and $\hat{\rho}^R_{Q_R/2,\,l}$ to estimate θ_l. According to the geometric relationship between the target and the center of the receive antenna array, we have

$$x_l = \rho^R_{Q_R/2,l}\cos(\theta_l) + x_{R,Q_R/2}, \tag{53}$$

which, combined with $\hat{x}_l$, $\hat{\rho}^R_{M_R/2,\,l}$, indicates that

$$\hat{\theta}_l = \cos^{-1}\left(\frac{\bar{x}_l - x_{R,Q_R/2}}{\bar{\rho}^R_{Q_R/2,l}}\right). \tag{54}$$

To determine the rough position of the target, the azimuth and distance information are needed. The azimuth information $\hat{\theta}_l$ is estimated and the distance information is contained in $\hat{\tau}_{M_T/2,\,Q_R/2,\,l}$. Thus, in the following, we use the estimated $\hat{\theta}_l$ and delay $\hat{\tau}_{M_T/2,\,Q_R/2,\,l}$ to jointly derive x_l and $\rho^R_{Q_R/2,\,l}$

Substituting the estimated parameters $\hat{\theta}_l$ and $\hat{\tau}_{M_T/2,\,Q_R/2,\,l}$ into Eqs. (53) and (36), respectively, we have

$$\begin{cases} x_l = \rho^R_{Q_R/2,l}\cos\left(\hat{\theta}_l\right) + x_{R,Q_R/2} \\ \rho^R_{Q_R/2,l} = c\hat{\tau}_{M_T/2,Q_R/2,l} - \sqrt{\left(\rho^R_{Q_R/2,l}\right)^2 + 2x_l\xi}. \end{cases} \tag{55}$$

Solving Eq. (55), we arrive at

$$\breve{\rho}^R_{Q_R/2,l} = \frac{\left(c\hat{\tau}_{M_T/2,Q_R/2,l}\right)^2 + 2\xi^2}{2c\hat{\tau}_{M_T/2,Q_R/2,l} - 2\cos\hat{\theta}_l\xi},$$

$$\breve{x}_l = \breve{\rho}^R_{Q_R/2,l}\cos\left(\hat{\theta}_l\right) + x_{R,Q_R/2}.$$

This completes the proof.

Contributors

Lingxiang LI and Ke LIU designed the research. Weixin CHEN and Qiang XU processed the data, Shengfu ZHAO drafted the manuscript. Zhen WANG helped organize the manuscript. Lingxiang LI and Zhi CHEN revised and finalized the paper.

Conflict of interest

Ke LIU, Shengfu ZHAO, Weixin CHEN, Zhen WANG, Lingxiang LI, Zhi CHEN, and Qiang XU declare that they have no conflict of interest.

References

Akyildiz IF, Kak A, Nie S, 2020. 6G and beyond: the future of wireless communications systems. *IEEE Access*, 8:133995-134030. https://doi.org/10.1109/ACCESS.2020.3010896

Akyildiz IF, Han C, Hu ZF, et al., 2022. Terahertz band communication: an old problem revisited and research directions for the next decade. *IEEE Trans Commun*, 70(6):4250-4285. https://doi.org/10.1109/TCOMM.2022.3171800

Alhafid AK, Younis S, Ali YEM, 2024. Enhanced far-field localization scheme using multi-ris and efficient beam sweeping. *Prog Electromagn Res C*, 140:163-175. https://doi.org/10.2528/PIERC23112903

Chen H, Sarieddeen H, Ballal T, et al., 2022. A tutorial on terahertz-band localization for 6g communication systems. *IEEE Commun Surv Tutorials*, 24(3):1780-1815. https://doi.org/10.1109/COMST.2022.3178209

Chen HY, Ahmad F, Vorobyov S, et al., 2021. Tensor decompositions in wireless communications and MIMO radar. *IEEE J Sel Top Signal Process*, 15(3):438-453. https://doi.org/10.1109/JSTSP.2021.3061937

Cohen D, Cohen D, Eldar YC, et al., 2018. SUMMeR: sub-nyquist MIMO radar. *IEEE Trans Signal Process*, 66(16):4315-4330. https://doi.org/10.1109/TSP.2018.2838541

Cui MY, Wu ZD, Lu Y, et al., 2023. Near-field MIMO communications for 6g: fundamentals, challenges, potentials, and future directions. *IEEE Commun Mag*, 61(1):40-46. https://doi.org/10.1109/MCOM.004.2200136

Da Rosa Zanatta M, De Mendonça FLL, Antreich F, et al., 2019. Tensor-based time-delay estimation for second and third generation global positioning system. *Digital Signal Process*, 92:1-19. https://doi.org/10.1016/j.dsp.2019.04.003

De Lathauwer L, 2006. A link between the canonical decomposition in multilinear algebra and simultaneous matrix diagonalization. *SIAM J Matrix Anal Appl*, 28(3):642-666. https://doi.org/10.1137/040608830

Gaudio L, Kobayashi M, Bissinger B, et al., 2019. Performance analysis of joint radar and communication using OFDM and OTFS. IEEE Int Conf on Communications Workshops, p.1-6. https://doi.org/10.1109/ICCW.2019.8757044

Knill C, Roos F, Schweizer B, et al., 2019. Random multiplexing for an MIMO-OFDM radar with compressed sensing-based reconstruction. *IEEE Microw Wireless Compon Lett*, 29(4):300-302. https://doi.org/10.1109/LMWC.2019.2901405

Li X, Chang B, Chen Z, 2023. Tensor decomposition based THz channel estimation in OTFS for integrated sensing and communications. IEEE Global Communications Conf, p.3996-4001. https://doi.org/10.1109/GLOBECOM54140.2023.10437761

Liu YJ, Liao GS, Yang ZW, et al., 2017. Design of integrated radar and communication system based on MIMO-OFDM waveform. *J Syst Eng Electron*, 28(4):669-680. https://doi.org/10.21629/JSEE.2017.04.06

Pan YJ, De Bast S, Pollin S, 2021. Indoor direct positioning with imperfect massive MIMO array using measured near-field channels. *IEEE Trans Instrum Meas*, 70:1-11. https://doi.org/10.1109/TIM.2021.3067963

Podkurkov I, Hamidullina L, Traikov E, et al., 2018. Tensor-based near-field localization in bistatic mimo radar systems. 22nd Int ITG Workshop on Smart Antennas, p.1-8.

Podkurkov I, Seidl G, Khamidullina L, et al., 2021. Tensor-based near-field localization using massive antenna arrays. *IEEE Trans Signal Process*, 69:5830-5845.

unedited

https://doi.org/10.1109/TSP.2021.3105797

Rinchi O, Elzanaty A, Alouini MS, 2022. Compressive near-field localization for multipath ris-aided environments. *IEEE Commun Lett*, 26(6):1268-1272. https://doi.org/10.1109/LCOMM.2022.3151036

Sakhnini A, De Bast S, Guenach M, et al., 2022. Near-field coherent radar sensing using a massive MIMO communication testbed. *IEEE Trans Wireless Commun*, 21(8):6256-6270. https://doi.org/

Sanson JB, Castanheira D, Gameiro A, et al., 2019. High-resolution DOA estimation of closely-spaced and correlated targets for MIMO OFDM radar-communication system. IEEE Int Symp on Phased Array System & Technology, p.1-5. https://doi.org/10.1109/PAST43306.2019.9021057

Sarieddeen H, Alouini MS, Al-Naffouri TY, 2021. An overview of signal processing techniques for terahertz communications. *Proc IEEE*, 109(10):1628-1665. https://doi.org/10.1109/JPROC.2021.3100811

Singh PR, Wang Y, Chargé P, 2016. Bistatic MIMO radar for near field source localisation using PARAFAC. *Electron Lett*, 52(12):1060-1061. https://doi.org/10.1049/el.2015.4380

Singh PR, Wang YD, Chargé P, 2017. Near field targets localization using bistatic MIMO system with spherical wavefront based model. 25th European Signal Processing Conf, p.2408-2412. https://doi.org/10.23919/EUSIPCO.2017.8081642

Temiz M, Alsusa E, Baidas MW, 2021. Optimized precoders for massive MIMO OFDM dual radar-communication systems. *IEEE Trans Commun*, 69(7):4781-4794. https://doi.org/10.1109/TCOMM.2021.3068485

Tian TW, Zhang TX, Kong LJ, et al., 2021. Transmit/receive beamforming for MIMO-OFDM based dual-function radar and communication. *IEEE Trans Veh Technol*, 70(5):4693-4708. https://doi.org/10.1109/TVT.2021.3072094

Tsujimura K, Mori H, 2022. Near field DoA estimation utilizing a large aperture MIMO array radar with Tx beamforming. 18th European Radar Conf, p.137-140. https://doi.org/10.23919/EuRAD50154.2022.9784552

Wan T, Liu Q, Du XF, et al., 2023. Performance analysis of joint range and velocity estimator for e-band ISAC. IEEE Wireless Communications and Networking Conf, p.1-5. https://doi.org/10.1109/WCNC55385.2023.10118736

Xiao M, Mumtaz S, Huang YM, et al., 2017. Millimeter wave communications for future mobile networks. *IEEE J Sel Areas Commun*, 35(9):1909-1935. https://doi.org/10.1109/JSAC.2017.2719924

Zhang HY, Shlezinger N, Guidi F, et al., 2022. Near-field wireless power transfer for 6g internet of everything mobile networks: opportunities and challenges. *IEEE Commun Mag*, 60(3):12-18. https://doi.org/10.1109/MCOM.001.2100702

Zhang HY, Shlezinger N, Guidi F, et al., 2023. 6G wireless communications: from far-field beam steering to near-field beam focusing. *IEEE Commun Mag*, 61(4):72-77. https://doi.org/10.1109/MCOM.001.2200259

Zhang JA, Liu F, Masouros C, et al., 2021. An overview of signal processing techniques for joint communication and radar sensing. *IEEE J Sel Top Signal Process*, 15(6):1295-1315. https://doi.org/10.1109/JSTSP.2021.3113120

Zhang RY, Cheng L, Wang S, et al., 2023. Target sensing in wideband massive MIMO-ISAC systems in the presence of beam squint. IEEE Int Conf on Communications Workshops, p.931-936. https://doi.org/10.1109/ICCWorkshops57953.2023.10283625

Zhang XF, Chen WY, Zheng W, et al., 2018. Localization of near-field sources: a reduced-dimension music algorithm. *IEEE Commun Lett*, 22(7):1422-1425. https://doi.org/10.1109/LCOMM.2018.2837049

Zhao BB, Hu KK, Wen FX, et al., 2023. TDLoc: passive localization for MIMO-OFDM system via tensor decomposition. *IEEE Internet Things J*, 10(23):20819-20833. https://doi.org/10.1109/JIOT.2023.3283991

Zuo WL, Xin JM, Liu WY, et al., 2019. Localization of near-field sources based on linear prediction and oblique projection operator. *IEEE Trans Signal Process*, 67(2):415-430. https://doi.org/10.1109/TSP.2018.2883034

unedited